5th Flow Control Conference
28 June - 1 July 2010, Chicago, Illinois

AIAA 2010-4982

Thrust Measurement of Dielectric Barrier Discharge Plasma Actuators and Power Requirements for Aerodynamic Control

Joseph W. Ferry[1] and Joshua L. Rovey[2]
Missouri University of Science & Technology, Rolla, MO 65409

Plasma-based aerodynamic actuators can modify a flow field without the need for moving control surfaces or a source of pressurized air. Actuator power consumption and thrust production were measured for driving frequencies between 1 and 18 kHz, and for driving voltages of 6 and 9 kV peak to peak. The actuator consumed between 3 and 22 W, and produced thrust levels between 0.05 and 0.2 mN per meter span. A comparison of results showed good agreement between this work and previous authors' results. The actuator effectiveness (thrust produced per watt of power input) was found to range between 0.017 and 0.11 mN/W. The continuous power consumption of a DBD actuator-based control system was then estimated by modeling the actuators as jet flaps. The elevator jet flap strength required to trim a small aircraft in flight was determined. A 0.5 kg aircraft with 0.76 m^2 wing area required between 0.47 and 2.22 kW of power for trim. A 3 kg aircraft with 1.27 m^2 wing area required between 13.6 and 54.6 kW of power for trim. In the most challenging circumstances, flight at stall or max velocity, current battery capacities would allow these aircraft to maintain trimmed flight for only 73 seconds.

Nomenclature

α	=	Angle of attack, degrees
AR	=	Aspect ratio
c	=	Lifting surface chord, m
C_l	=	Infinite wing lift coefficient
C_L	=	Finite wing lift coefficient
$C_{L,\alpha=0}$	=	Lift Coefficient when $\alpha = 0$
$C_{L,h}$	=	Horizontal stabilizer lift coefficient
$C_{L,w}$	=	Main wing lift coefficient
$C_{M,cg}$	=	Aircraft moment coefficient about the center of gravity
$C_{M,w}$	=	Main wing moment coefficient when $\alpha = 0$
C_μ	=	Jet flap momentum coefficient
δ	=	Jet flap deflection angle, degrees
ε_h	=	Downwash angle at horizontal stabilizer, degrees
η_h	=	Ratio of free stream dynamic pressure to dynamic pressure at horizontal stabilizer
F	=	Ratio of finite and infinite wing lift coefficients
F_{trim}	=	Jet momentum required to trim the aircraft in steady level flight, mN
F/P	=	Actuator effectiveness, mN/W
i_w	=	Wing incidence angle, degrees
L_{tail}	=	Horizontal stabilizer lift, N
L_{wing}	=	Main wing lift, N
m_i	=	Jet flap mass flow rate, kg/s
M_{wing}	=	Moment produced by the main wing, N-m

[1] Graduate Research Assistant, Aerospace Plasma Laboratory, Mechanical & Aerospace Engineering, 210 Toomey Hall, 400 W. 13th St., Student Member AIAA.
[2] Assistant Professor of Aerospace Engineering, Mechanical & Aerospace Engineering, 292D Toomey Hall, 400 W. 13th St., Senior Member AIAA.

μ = Measurement true mean value
n = Number of samples in a measurement sample set
P_{trim} = Power required to trim the aircraft in steady level flight, W
q = Free stream dynamic pressure, Pa
S = Measurement set standard deviation
S_h = Horizontal stabilizer area, m^2
S_w = Main wing area, m^2
V = Aircraft flight velocity, m/s
v_i = Jet flap induced velocity, m/s
$\overline{x}$ = Measurement sample set mean
x_i = Measurement single sample value
$\overline{X}_{ac,h}$ = Nondimensional distance from aircraft datum to horizontal stabilizer aerodynamic center
$\overline{X}_{ac,w}$ = Nondimensional distance from aircraft datum to wing aerodynamic center
$\overline{X}_{cg}$ = Nondimensional distance from aircraft datum to center of gravity

I. Introduction

DIELECTRIC barrier discharge plasma actuators are simple devices that include a dielectric layer between two electrodes in a specific arrangement. One electrode is grounded and covered by a dielectric layer and the other electrode is placed on top of the dielectric. These electrodes are designated as the covered and exposed electrodes, respectively. This configuration is shown in Figure 1. The dielectric layer can be any substance with insulating properties. The materials commonly used in research are Kapton polymer tape, Teflon tape, quartz glass, and Macor ceramic. The electrodes are typically made of copper foil tape.

To operate the actuator, a high voltage AC signal is applied to the exposed electrode. This causes a plasma discharge to form over the surface of the dielectric between the exposed and covered electrodes. The discharge causes an ionic wind to blow across the actuator. In still air, the actuator induces a flow that draws air toward the surface of the actuator, and accelerates this air downstream in a direction tangential to the dielectric. It is clear that the actuator itself forms and accelerates the plasma; the reaction force on the actuator is small but readily measured.

While plasma actuators are not yet capable of actuating high Reynolds number flows, actuator effectiveness has increased greatly through recent research efforts. It is likely that the first flight systems using DBD plasma actuators will be small remote vehicles operating at low Reynolds numbers. The light weight, simplicity, and fast reaction times of the actuators naturally lend themselves to this application. However, in any flight application the power supply and actuators must be considered together as a unit. The actuator driving circuitry must include an energy storage system, a signal generator, and a high-voltage step-up stage.

As the actuator power requirements increase, the weight of this power supply must necessarily also increase. Increased energy storage, heavier cabling, and greater cooling requirements would all contribute to this weight increase. Therefore, reducing the power requirements of the actuator would also reduce the weight of the power supply, and enable the systems to be mounted on smaller vehicles. The motivation for this research is to examine the power requirements for a DBD actuator-based control system.

DBD plasma actuators have been the subject of intense research recently. A major focus of the published work has been parametric optimization. In these studies authors have investigated how different operating parameters affect the thrust produced by DBD actuators. Enloe and Thomas have parametrically investigated operating voltage, operating frequency, applied waveform shape, dielectric type, and dielectric thickness with the aim of increasing actuator thrust.[1,2] In Enloe's work he found that altering the AC driving voltage waveform has a great effect on the actuator properties. He drove an actuator with a sawtooth waveform that maximized the time spent in the forward stroke, and, compared to a sawtooth of opposite polarity

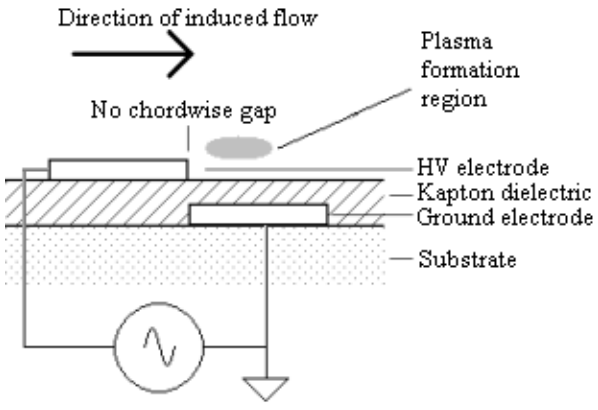

Figure 1: DBD actuator layout.

(which maximized the backward stroke), saw a considerable increase in actuator performance for the same power input. He also showed that using a sharper exposed electrode increased actuator performance, which he attributed to the higher electric field produced.

Thomas investigated the effect of different dielectric parameters on the actuator thrust production. He found that using thicker dielectrics allowed the use of higher actuator voltages, which increased thrust production. He also found that using dielectrics with low dielectric constants increased thrust production. With the same goal, Opaits has investigated DBD operation using pulsed waveforms[3] and Durscher and Roy have investigated novel actuator configurations.[4] Opaits found that pulsed waveforms were capable of performance similar to conventional sinusoidal-driven actuators at lower voltage levels. Durscher and Roy used a three-electrode configuration to increase actuator efficiency compared to the conventional configuration.

Some authors have investigated the plasma formation and acceleration processes that occur in DBD actuators. Enloe has investigated DBD plasma ignition and spread, and discharge asymmetry.[1,5] Stanfield has investigated ion concentration and temperature in the plasma.[6,7] Enloe and Font have investigated dielectric surface charge build-up and actuator force generation.[8,9] Each of these has contributed plasma property measurements to the literature. Font found that the presence of oxygen plays an important role in DBD force production, and that a charge build-up occurs on the surface of the dielectric downstream of the exposed electrode. This charge build-up can reach a potential of several kilovolts.

There has also been a focus on applications for DBD plasma actuators. This focus has been driven by the many advantages that DBD actuators offer designers. DBD actuators require none of the ducting that is required of traditional blowing or suction actuators. All that is needed is insulated electrical cabling. Additional advantages are the self-limiting nature of the discharge and the low power levels required to operate the device. Actuators with flexible dielectrics can be made to fit any surface shape. All of these reasons have contributed to a rapidly growing body of experimental work which focuses on specific applications for DBD actuators.

Some of the applications investigated include an active stall detection and control system,[10] bluff body noise control,[11] plasma-enhanced combustion,[12] jet mixing enhancement,[13] high angle-of-attack separation control,[14] high angle-of-attack roll control,[15] turbine blade separation control,[16] DBD microthrusters,[17] turbine tip gap flow control,[18] and other air flow control applications.[19-23] Other developments in DBD actuator research have been summarized in a review article by Corke, Enloe, and Wilkinson.[24]

The work presented here has two main objectives. The first is to perform an experimental study of the efficiency of a DBD plasma actuator. The actuator thrust and power consumption are measured for this calculation. This has been done previously, but this work increases the base of experimental data available. The second objective is to examine the problem of a plasma actuator-based control system, and to estimate the power required for such a system to trim a small aircraft in level flight. For a stable aircraft in level flight the only control requirement is the elevator trim. Therefore this power requirement is an adequate estimate of the control system power requirement in flight.

II. Experimental Setup and Equipment

To investigate the plasma actuator thrust and power consumption, the experimental setup needed to meet three requirements. First, the plasma actuator needed to be powered by a supply capable of producing a 9 kVp-p waveform while supplying 20-30 watts of power. Second, the experiment needed to be able to measure the actual power input to the actuator. Third, the experiment needed to be able to measure the thrust produced by the plasma actuator operation.

The experimental concept used was similar to those used in previous studies.[6] The actuator was powered by an audio amplifier and high-voltage step-up transformer. The actuator voltage and current waveforms were measured by a high voltage probe and a Pearson current monitor. The actuator electrical supply and measurement system is shown in Figure 2.

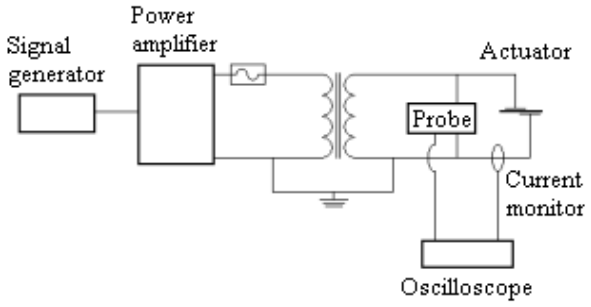

Figure 2: Actuator electrical supply and measurement system.

The actuator thrust was measured by a balance beam attached to a laboratory mass balance. Because the actuator thrust was extremely small, the balance beam was arranged so that it would mechanically amplify the force produced by the actuator. This arrangement is shown in Figure 3. The counterweight allowed the beam

to be balanced so that the scale was not overloaded. The actuator power wires were made of lightweight, flexible wires and attached at the balance beam point of rotation.

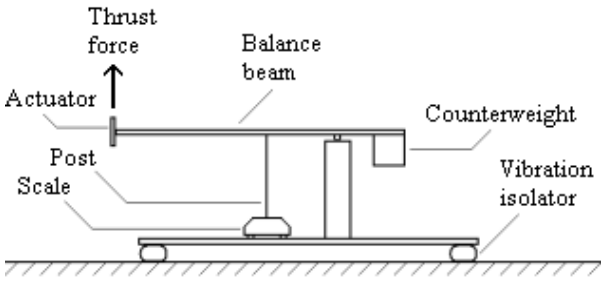

Figure 3: Balance beam thrust measurement setup.

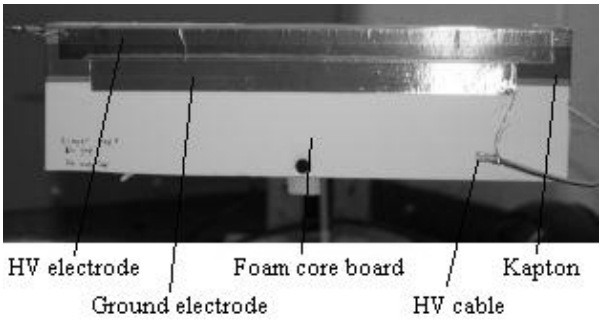

Figure 4: Actuator top view, as mounted on the test stand.

A. Actuators

The actuators used in this study were constructed by hand, and used copper tape electrodes with a Kapton tape dielectric. The dielectric was constructed by layering three pieces of Kapton on top of each other, which resulted in a dielectric thickness of 0.2 mm. The electrodes were positioned so that the electrodes did not overlap each other, but the exposed electrode edge lay directly on top of the covered electrode edge (Fig. 1). The actuators were mounted on a foam-core board substrate. The exposed electrodes were each 25 cm in length, and the covered electrodes were slightly longer than the exposed electrodes (Fig. 4).

B. Power Supply

The actuator driving circuitry had three main components. A Wavetek Model 110 analog function generator was used to drive a Crown CE2000 amplifier. The function generator was used to define the waveform shape, signal amplitude, and driving frequency. The CE2000 was a two-channel amplifier and each channel was rated to provide 975 W to a 2-ohm load. The amplifier was operated in a dual mono configuration, so that one of the amplifier channels drove the actuator while the other was unused. The amplifier output drove a transformer which stepped up the voltage to kilovolt levels.

Two separate transformers were used to drive the actuator across different frequency ranges. The first was a Corona Magnetics CMI-6495 transformer with a 1:100 turns ratio. It is rated for a 4000 V, 0.03 A output. Its self resonant frequency was near 3 kHz, and it was used to drive the actuator for frequencies between 1-10 kHz. The second transformer was a Corona Magnetics CMI-5012-1. It had a 1:137.5 turns ratio, and it was rated for a 5500 V, 0.1 A output. Its self resonant frequency was 6 kHz, and it was used to drive the actuator for frequencies between 10-18 kHz. Both of these transformers were protected by a 5 A fuse between the amplifier and the transformer primary coil.

C. Electrical Measurement

In the experiment, a common ground was provided between the amplifier output, the transformer primary coil, and the transformer secondary coil. To accurately measure the actuator driving voltage, a Tektronix P6015 high voltage probe was used to measure the voltage between the actuator exposed electrode and ground. The probe was physically located as close to the electrode as possible, to eliminate the effects of corona on long wire runs. The probe -3 dB attenuation point is 75 MHz, so it was sufficient to measure the 1-18 kHz applied voltage waveforms.

The actuator current was measured by placing a Pearson electronics model 4100 current monitor around the actuator ground wire. This type of current monitor (a Rogowski coil) is essentially a coil of wire that encircles the wire under test, and it was designed so that the voltage induced in the monitor wire is proportional to the current through the test wire. The current was measured through the ground wire because capacitive effects between the monitor and high voltage wire would introduce error to the measurement if the high voltage line were measured. The current monitor low frequency -3 dB attenuation point was 140 Hz, and the high frequency -3 dB attenuation point was 35 MHz. The current monitor also had a usable rise time of 10 ns. This means that the current monitor was able to accurately measure displacement current at the 1 kHz driving frequency and was also able to capture the microdischarge current spikes produced by the actuator.

The high voltage probe and current monitor were both connected to a Tektronix TDS 2014B 100 MHz oscilloscope. The oscilloscope interfaced with a PC via USB, and a LabVIEW program was used to capture and store each waveform.

D. Thrust Measurement

An Ohaus SP-123 mass balance was used to measure the actuator thrust. This balance had a 0.001 gram resolution and could measure a maximum of 120 grams. This corresponds to a 10^{-6} N resolution and maximum measurable force of 1.17 N. Because the actuator thrust was extremely small, a balance beam was used to multiply the actuator force. Most of the balance beam weight was supported by a rolling support that was free to rotate, and a second support rested on the balance measurement tray. A counterweight was positioned so that the balance was not overloaded. The force measured by the balance was then 4.9 times greater than the actual actuator thrust produced. To power the actuator, two electrical leads had to be attached to the balance beam. So that they would not influence the measurement, these leads were made as lightweight as possible and were attached close to the point of rotation of the beam. With this setup, they exerted a moment on the beam that was as close as possible to zero.

The thrust measurement setup was very sensitive, so that it was possible for ambient air currents to introduce thrust measurement noise that was many times greater than the actual force being measured. To eliminate this noise the entire setup was set inside an isolating chamber. The chamber was a cylinder 8 feet long and 4 feet in diameter, large enough so that the actuator would not set up a large scale circulating airflow inside the chamber.

III. Experimental Observations and Results

This section begins with qualitative observations of the actuator and plasma. It contains the experimental method and the experimental data gathered. The measurements reported include power measurements, thrust measurements, a comparison of results with other authors, and actuator efficiency calculations.

A. Visual Observations of the Plasma Discharge

Several visual observations were made of the plasma structure during actuator operation. It is well-known that a diffuse-mode barrier discharge will transition to a highly filamentary discharge as the driving voltage and frequency are increased. The point at which the discharge transitions to the filamentary mode depends upon the electrode spacing, dielectric thickness, and dielectric material. The filamentary mode discharge appears when localized hot spots appear in the plasma. These hot spots appear as brighter regions of the plasma because of increased plasma formation in the hot spots.

When the discharge was already in a filamentary mode, increasing the actuator operating frequency increased the number of hot spots in the plasma. With the actuators used in this study, the presence of hot spots also typically indicated that the actuator driving voltage was near the maximum permitted by the dielectric. Therefore, increasing the driving voltage from this point resulted in actuator failure due to dielectric burn-through.

A visual survey of the DBD plasma is useful because the thrust and effectiveness of the plasma actuator heavily depended upon the kind of discharge that was created. As the actuator driving voltage and frequency were increased, the actuator thrust increased whether the discharge was in a diffuse or a filamentary mode. However, when the discharge was in a filamentary mode the actuator efficiency decreased as the driving frequency was increased. Each of the photos in Figures 5 and 6 was taken by a Canon Rebel DSLR camera. For each photograph, an f/10 aperture and ¼ second shutter speed was used.

It can be seen that when the driving voltage was 6 kVp-p, the discharge was relatively diffuse over the

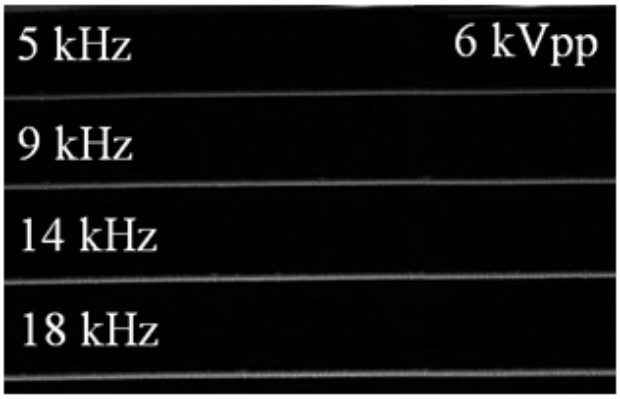

Figure 5: The plasma discharge at 6kVp-p.

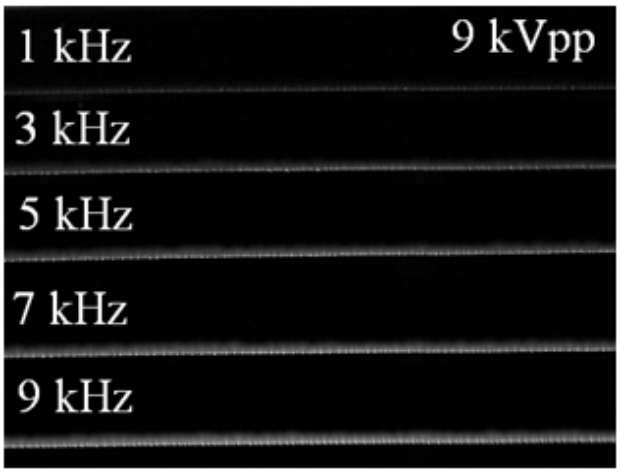

Figure 6: The plasma discharge at 9 kVp-p.

entire range of frequencies used (Figure 5). The plasma intensity increased as the driving frequency was increased, but hot spots never formed in the discharge. The difference between Figures 5 and 6 is significant. Figure 6 shows the discharge when the driving voltage was 9 kVp-p. At a driving frequency of 1 kHz, some barely-formed hot spots were observed. When the frequency was increased to 3 kHz, hot spots formed and were plainly visible. As the frequency was increased to 9 kHz, the number and intensity of the hot spots increased significantly. At these higher frequencies, the discharge was highly filamentary.

B. Experimental Method and Data Acquisition

During the experiment, three separate sets of data were recorded. The first of these was the actuator thrust measurements. A LabVIEW program was used to record the thrust data. It recorded the force balance readout approximately five times per second, as fast as the scale circuitry allowed.

It was found that the force measurement would drift over time. This drift displayed unusual characteristics, and one significant observation was that the measurement drifted in one direction with the actuator off and in the opposite direction with the actuator on (Figure 7). For this reason it is believed that the drift was related to the actuator operation in some way. Other experiments showed that the drifting was also related to the room ambient conditions. The cause of this drifting is unknown, but it prevented the acquisition of thrust measurements simply by taking a quiescent value and a second measurement with the actuator on.

To eliminate the drift effect from the measurements, the actuator thrust measurement was taken by turning off the actuator and measuring the change in force that resulted. Five separate force readings were taken for each measurement.

The second and third measurements taken were the actuator applied voltage and current measurements. Again a LabVIEW program was used to simultaneously acquire and store both current and voltage waveforms. For each measurement, 100 separate voltage and current waveforms were recorded.

To summarize, each measurement followed this procedure:

1. Set the actuator driving frequency
2. Use LabVIEW to begin recording force measurements from the mass balance
3. Turn on the power amplifier
4. Increase the voltage amplitude to the desired value
5. Use LabVIEW to record 100 voltage and current waveforms
6. Quickly decrease the voltage amplitude to 0 V
7. Allow the scale reading to settle
8. Repeat steps 4-7 four more times
9. Turn off the power amplifier
10. Stop and save the LabVIEW force measurement record

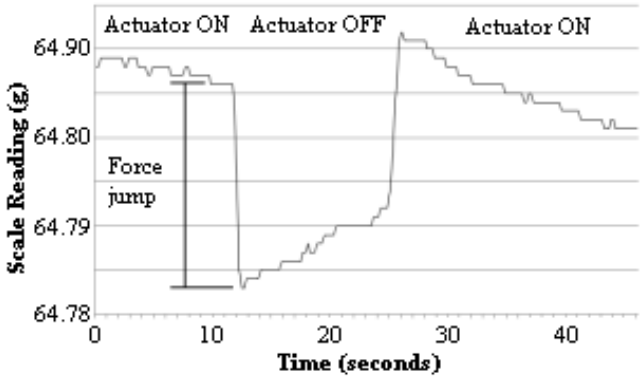

Figure 7: Force trace drift and measurement drop.

C. Power Consumption Results

Actuator power consumption is presented in this section. Figure 8 shows how the actuator power consumption changes as the applied frequency changes. The applied voltage is held constant at 6 kV peak to peak and 9 kV peak to peak. The points on each chart represent the mean power consumption, calculated from five sets of 100 waveforms each. The error bars shown are the 99% confidence interval for the measurement average.

The experimental apparatus did not directly measure power input, but it recorded the driving voltage and current waveforms. To calculate the power the voltage and current waveforms were multiplied point-by-point, which gave a power waveform. The power input was calculated by averaging the power waveform over one or two periods of the driving frequency.

There are two distinct regions in the 6 kVp-p set of data. For driving frequencies between 5 – 10 kHz the power consumption increases linearly as the driving frequency increases. There is a small discontinuity between 10 and 11 kHz, and between 11 – 18 kHz driving frequencies the power consumption begins to level off. The discontinuity is explained by the fact that two different power transformers were used to power the actuator. One transformer powered the actuator between 5 – 10 kHz, and the second transformer powered the actuator between 11 – 18 kHz. The transformers that were used are highly resonant devices, and when operated away from their self resonant frequency, the driving voltage waveforms were not perfect sine waves.

Each transformer provided a slightly different driving voltage waveform, which altered the plasma discharge characteristics. When the discharge was modified, the power consumption also changed. It is clear then that distortions of the applied voltage waveform are a source of bias error in the experiment. In the 9 kVp-p data no discontinuity is present. This is because the same transformer powered the actuator for all of the measurements. At the higher driving voltage it is again observed that the power consumption increases linearly with the driving frequency.

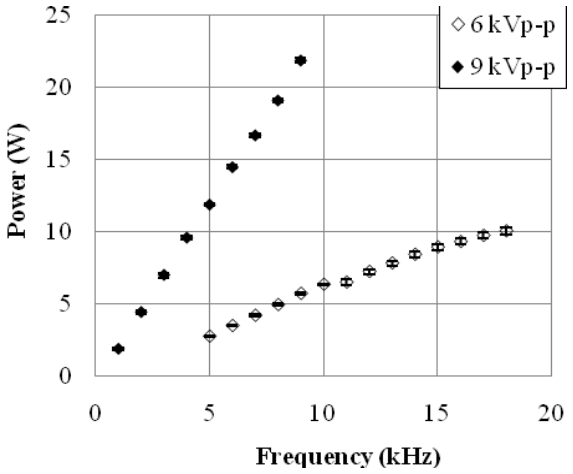

Figure 8: Actuator power consumption with 99% CI error bars shown.

D. Thrust Measurement Results

Measured actuator thrust is presented in this section. Figure 9 shows how the actuator thrust changes as the applied frequency changes. The applied voltage is held constant at 6 kV peak to peak and 9 kV peak to peak, respectively. Each data point represents the average thrust value over five separate trials. The error bars shown are the 99% confidence interval for the measurement average.

Figure 9 shows actuator thrust levels when the applied voltage is held constant at 6 kV peak to peak and 9 kV peak to peak. In the 6 kV peak to peak data set the error bars appear to be quite large relative to the value of the measurement. This is because the resolution of the overall experimental setup is about 0.008 mN/m. This is an order of magnitude smaller than the lowest thrust measurement. There are no significant features on this chart because the discharge was operating in the diffuse mode over the entire range of measurement. Therefore, the effects of the transition to filamentary mode discharge are not seen here. The discontinuity that was seen in Figure 8 is not present here. However, the discontinuity may be masked by the greater effects of measurement error in this set of data.

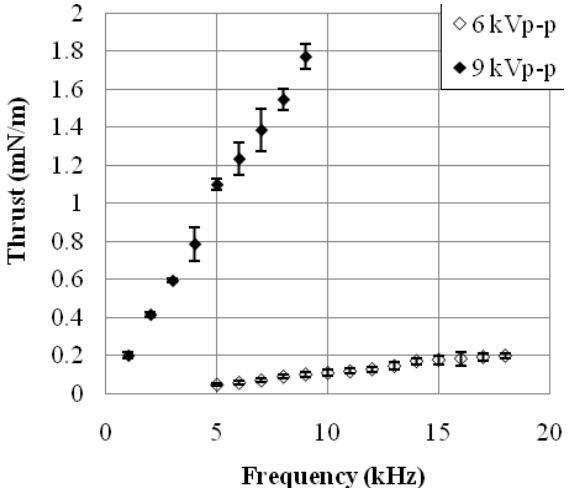

Figure 9: Actuator thrust production with 99% CI error bars shown.

When the applied voltage is held constant at 9 kV peak to peak there are no significant features in the data set because the actuator was operating in the filamentary discharge mode over the entire measurement range. The measurements in this chart were taken in two separate sets on two different days, and different actuators were used to take the two sets of data. One actuator was used for the 1 – 4 kHz range, and a second actuator was used for the 5 – 9 kHz range. This shows that the thrust measurements were relatively insensitive to the small differences between two hand-built actuators.

E. Thrust Results Comparison With Literature

There are not yet any theoretical models that can predict actuator performance, so to assess the validity of this experimental data set it was compared with thrust measurements that other authors have published. Figure 10 contains thrust measurements taken from the current work as well as literature data. In this figure, the 6 kVp-p data set appears to be almost horizontal. This is because the thrust levels at this voltage are extremely low compared to the other data sets. The 9 kVp-p data set is just below the 12.6 kVp-p measurements reported by Enloe.[2] The difference is smaller than what would be expected, but differences in the driving voltage waveform, actuator geometry, and dielectric material could account for the difference. The single data point reported by Takagaki does not appear to fit with any of the other data.

F. Actuator Effectiveness Results

One actuator property that is of interest is how efficiently the actuator converts electrical power into fluid jet power. However, finding the actual power transferred to the fluid would require both a thrust measurement and the induced flow velocity. Measuring the latter quantity is not a trivial problem, so instead of finding the true actuator power conversion efficiency, a quantity called the actuator effectiveness is used instead. The actuator effectiveness, F/P, is defined as the actuator static thrust divided by the actuator power consumption. The physical meaning of an effectiveness value is that it shows how much momentum can be added to the flow for one unit of power input. This quantity has been reported in the literature,[2,5] but has not always been explicitly named.

Calculated actuator effectiveness is presented in this section. Figure 11 shows how the actuator effectiveness changes as the applied frequency changes. The applied voltage is held constant at 6 kV peak to peak and 9 kV peak to peak, respectively. Each data point represents the average effectiveness value over five separate trials. The error bars shown are the 99% confidence interval for the measurement average.

At 6 kV peak to peak, it is seen that the actuator effectiveness is nearly constant with changing frequency. This actuator was operating in the diffuse mode of discharge across the entire range of measurement. There appears to be no significant effect from switching transformers between 10 and 11 kHz. Because it was possible to measure the power to a very high degree of confidence, the size of the error bars here are dominated by the thrust measurement error.

At 9 kV peak to peak, one actuator was used to find the effectiveness between 1 – 4 kHz, and a second actuator was used to find the effectiveness between 5 – 9 kHz. It is apparent that for both of these actuators the effectiveness increased as the driving frequency was decreased. However, the trends do not meet between the two data sets. This suggests that the actuator effectiveness is either highly sensitive to small changes in the actuator layout, or that it is sensitive to the ambient conditions.

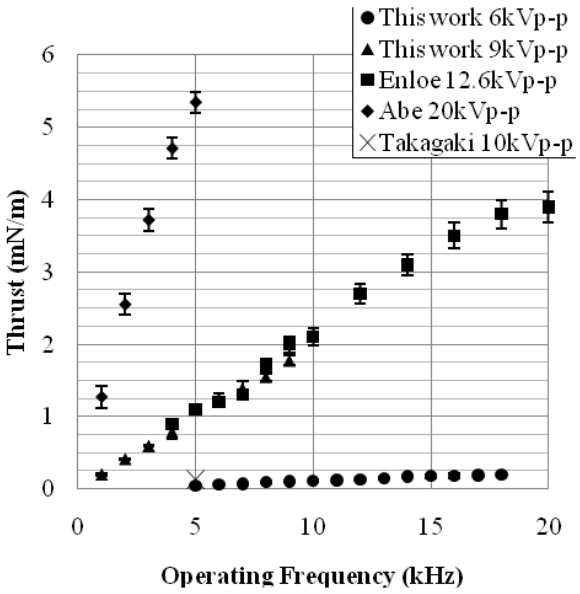

Figure 10: Actuator thrust measurement compared with other authors. Data reproduced from refs. 2, 25, and 26.

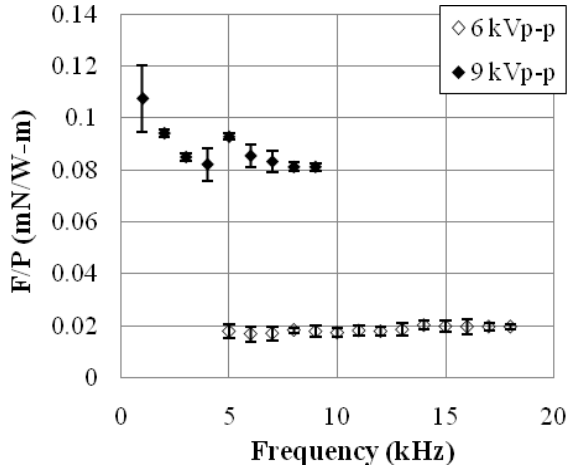

Figure 11: Actuator effectiveness with 99% CI error bars shown.

G. Error Quantification in the Experimental Results

Care was taken not to introduce any bias error by poor experimental technique, but because there is no accepted value for the actuator thrust measurements it was not possible to quantify whether any bias error was present in the experimental data.

One source of random error in the experiment was the waveform generator used to set the driving frequency and voltage. The waveform generator was an analog device, and the voltage and frequency for each measurement was set by hand. When a thrust value at 9 kVp-p and 5 kHz is given, these are the nominal voltage and frequency values. The actual experiment voltage and frequency will have differed slightly from the nominal case. Other sources of possible random error include electrical noise in the measurement setup and physical vibrations causing noise in the thrust measurement.

The random thrust measurement error was quantified by applying Student's t-distribution to find measurement confidence intervals. The t-distribution was used because each mean thrust value was found by averaging five data

points. The calculation method taken from reference 27 shows that for a data set consisting of five samples, it is 99% certain that the true mean of the experimental measurement is contained within the interval defined by Eqn. 1.

$$\mu = \bar{x} \pm 4.604 \frac{S}{\sqrt{5}} \tag{1}$$

Because each average power measurement was based on 100 separate data points, a normal distribution was used to find the confidence interval for these measurements. For a normal distribution and a data set with 100 samples, it is 99% certain that the true mean of the experimental measurement is contained within the interval given by Eqn. 2. For both of these calculations, the sample mean and standard deviation are calculated using Eqn. 3 and 4, respectively.

$$\mu = \bar{x} \pm 2.575 \frac{S}{\sqrt{100}} \tag{2}$$

$$\bar{x} = \sum_{i=1}^{n} \frac{x_i}{n} \tag{3}$$

$$S = \sqrt{\frac{\left(\sum_{i=1}^{n} x_i^2\right) - n\bar{x}^2}{n-1}} \tag{4}$$

It is emphasized that these confidence intervals reflect only the random error present in the experimental data. A confidence interval reflects only the spread of data as measured by this experiment. Therefore, a 99% confidence interval does not mean that the actual true value for actuator thrust lies within the interval, but that the average actuator thrust value measured by this experiment will lie within the interval 99 times out of 100. If there is no bias error present in the experiment, then it is 99% certain that the true actuator thrust value lies within the confidence interval.

IV. Actuator Power Consumption Required to Trim an Aircraft

This section presents an analysis of power requirements for a micro air vehicle control system based on DBD plasma actuators. The goal of the analysis was to find the continuous power required to trim the aircraft in steady level flight. The analysis is based upon two conventional micro air vehicles. One of these vehicles is a performance-optimized vehicle with a 1.27 m wingspan and 3 kg mass. The second vehicle is much smaller, with a 0.76 m wingspan and 0.5 kg mass. Table 1 gives a physical description of each aircraft.

The analysis proceeds as follows. First, the jet flap concept is introduced and its applicability to the problem at hand is demonstrated. Jet flap operation and governing equations are discussed. Next, the aircraft longitudinal trim problem is presented and solved for the elevator jet strength required to trim the aircraft in level flight. Last, the power requirement for these flight conditions is calculated using current experimental data.

Table 1: Aircraft Parameters

	Aircraft 1	Aircraft 2
mass [kg]	3	0.5
wing area [m^2]	1.27	0.76
tail area [m^2]	0.064	0.017
tail chord [m]	0.15	0.076
stall velocity [m/s]	10.7	11.0
static margin [% of chord]	16.6	19.5

A. Jet Flap Introduction

Powered pneumatic flow control technology was first investigated as early as the 1930s. While the implementation has taken many forms, jet flap systems traditionally feature a source of high-pressure air which can be blown across a conventional control surface or used to create a pure air jet. If the jet issues from the airfoil directly, it is called an internally blown flap. Figure 12 shows a schematic of a pure jet flap that was used to

construct the first theoretical models of jet flap aerodynamics.

Korbacher[29] provides an overview of jet flap operation and application to V/STOL flight. Jet flap systems operate on the principle of supercirculation. When the trailing edge jet is sufficiently strong, the Kutta condition at the trailing edge is relaxed. That is, the point in the flow where circulation goes to zero is pushed aft of the airfoil trailing edge.[30] The effect is similar to extending the airfoil chord. With an angled jet, the flow can be turned as well, increasing the effective camber of the airfoil. Because of these effects, the lift gained can be much greater than the jet thrust. Using jet flaps, wind tunnel experiments have achieved finite-wing lift coefficients greater than seven.[31] For V/STOL flight, the advantage of such a system is apparent.

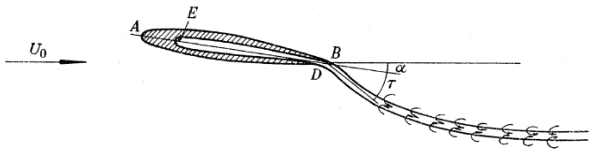

Figure 12: The internally blown pure jet flap considered by Spence. Reproduced from reference 28.

B. Jet Flap Theory

Spence[28] first formulated a two-dimensional inviscid jet flap theory in 1956; Maskell and Spence presented a three-dimensional theory in 1959.[32] This work is based upon a textbook treatment of the jet flap by McCormick,[30] which is based on the original work by Spence and Maskell.

A question that needs to be addressed is whether the jet flap theory is applicable to the jets produced by DBD plasma actuators. Traditional jet flaps are positive mass flux devices that work by injecting a jet into the flow, while DBD plasma actuators are zero mass flux devices which locally accelerate the flow over the airfoil. However, Spence's model appears to be well-suited to analyzing DBD actuator jets. Spence considered a thin jet sheet, seen in Figure 12. He constructed the jet by considering the case where the jet thickness approaches zero and the jet exit velocity approaches infinity. In this limit, the jet mass flow rate approaches zero, while the jet momentum approaches a finite value. This model describes the situation with a trailing-edge DBD actuator very well. Additionally, later investigations found that the jet flap effect scales with the jet momentum, rather than the jet mass flow rate.[33] These investigations also found that the jet flap effect depended only weakly upon the jet thickness. This implies that the jet flap effectiveness is determined primarily by the distance it extends before it is turned in the direction of the free stream.

The nondimensional jet momentum coefficient, C_μ, is the primary factor in determining the jet effect upon the airfoil properties:

$$C_\mu = \frac{m_j v_j}{qc} \tag{5}$$

The quantity $m_j v_j$ is the jet momentum, and is equal to the reaction thrust produced by the jet. The jet flap theory results here are the result of lifting-line theory applied to jet flaps, and are reproduced from reference 29. The lift coefficient of a pure jet-flapped airfoil is given by:

$$C_l = \left(\frac{\partial C_l}{\partial \delta}\right)\delta + \left(\frac{\partial C_l}{\partial \alpha}\right)\alpha \tag{6}$$

$$\frac{\partial C_l}{\partial \delta} = [4\pi C_\mu (1 + 0.151 C_\mu^{1/2} + 0.139 C_\mu)]^{1/2} \tag{7}$$

$$\frac{\partial C_l}{\partial \alpha} = 2\pi (1 + 0.151 C_\mu^{1/2} + 0.219 C_\mu) \tag{8}$$

In the case where there is no jet (C_μ=0), it can be seen that the airfoil lift curve slope is then equal to that predicted by traditional lifting-line theory, $\partial C_l/\partial \alpha = 2\pi$. An important result of these equations is that a DBD plasma actuator based control system will require some mechanism to turn the jet. It can be seen that if δ=0, then the jet will only have the effect of increasing the lift curve slope $\partial C_l/\partial \alpha$. For an airfoil with a fixed positive angle of attack α>0 and jet deflection δ=0, turning on the jet can increase the section lift, but not decrease it.

Fortunately, there are ways to produce an angled jet flap without resorting to mechanical deflection surfaces. Figure 13 presents one possibility. It relies on the Coanda effect to turn the jet through the appropriate angle. Previous investigations have shown the feasibility of using the Coanda effect to turn trailing edge jets through significant angles even for jets with small values of C_μ.[34]

Last in the discussion of jet flap theory is the relation of finite and infinite wing lift coefficients. These are related by a factor, F, given as Eqn. 9.

$$F = \frac{C_L}{C_l} = \frac{AR + 2C_\mu/\pi}{AR + 2 + 0.604C_\mu^{1/2} + 0.876C_\mu} \quad (9)$$

This is an approximation, valid for jet-flapped surfaces with large aspect ratios, AR, and small jet momentum coefficients, C_μ. An implicit relation to find exact values for F is available, but it is inconvenient to use.

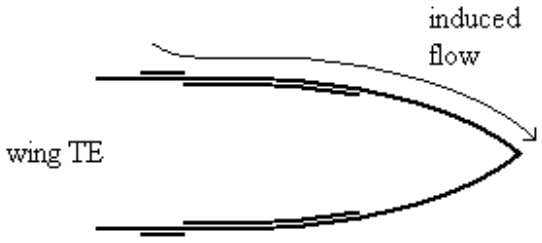

Figure 13: A proposed Coanda effect jet flap. The thick lines represent DBD actuator electrodes.

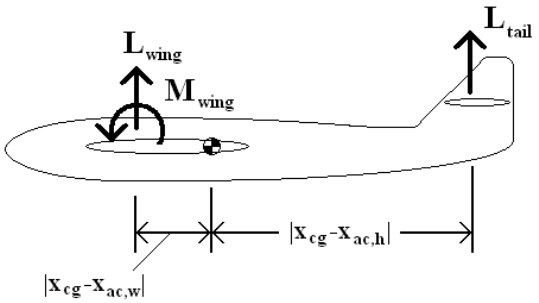

Figure 14: A simplified aircraft free body diagram.

C. Aircraft Longitudinal Trim

For a conventional aircraft, the longitudinal trim problem can be posed as such: given the physical parameters of an aircraft and its forward velocity, what combination of aircraft angle of attack and elevator deflection produce a zero moment about the aircraft center of gravity? For a stable aircraft in straight and level flight the only control force required is an elevator trim deflection. The problem is similar for an aircraft with a plasma jet control system, but an elevator jet momentum is sought instead of an elevator flap deflection. This simple analysis considers only three forces, which are shown in figure 14.

Disregarding any moment contribution by the aircraft propulsion or fuselage, the aircraft moment coefficient about its center of gravity is given by Eqn. 10.

$$C_{M,cg} = C_{L,w}(\overline{X_{cg}} - \overline{X_{ac,w}}) + C_{M,w} + \eta_h \frac{S_h}{S_w} C_{L,h}(\overline{X_{cg}} - \overline{X_{ac,h}}) \quad (10)$$

$$C_{L,w} = C_{L,\alpha=0} + \frac{\partial C_{L,w}}{\partial \alpha}(\alpha + i_w) \quad (11)$$

$$C_{L,h} = C_{L,\alpha=0} + \frac{\partial C_{L,h}}{\partial \alpha}\left(\alpha + i_w - \varepsilon_{h,\alpha=0} - \frac{\partial \varepsilon}{\partial \alpha}\alpha_w\right) + \frac{\partial C_{L,h}}{\partial \delta_e}\delta_e \quad (12)$$

For the plasma jet flap elevator, the lift coefficient derivatives are given by equations 7-9 above. The goal of this analysis is to create a plasma jet-based control system that is equivalent to the conventional control system already installed on the aircraft. With this in mind, the following process was used. First, the trim α and δ_e were calculated for the conventional aircraft configuration, at the free stream velocity of interest. Then the free stream velocity and aircraft angle of attack were held constant, and the jet momentum coefficient required to satisfy the trim condition ($C_{M,cg}$=0) was found. For these calculations, it was assumed that the plasma jet deflection δ=±10°.

D. Trim Calculation Results

Results are summarized in Table 2. There are three conditions of primary interest for trimmed flight. These conditions are trimmed flight at $V=V_{stall}$, trimmed flight during cruise, and trimmed flight at $V=V_{max}$, the maximum attainable velocity in straight and level flight. Flight at the stall velocity and maximum velocity represent the conditions where the maximum elevator control inputs are required. The tail incidence angle for both aircraft was set so that no elevator input was required at the cruise velocity of 16 m/s. The maximum velocity for both aircraft was assumed to be 33.5 m/s.

Table 2: Jet momentum required to trim the aircraft.

		V (m/s)	α (degrees)	δ (degrees)	$C_{\mu,trim}$	Jet momentum (N/m)
V_{stall}	Aircraft 1	10.7	8.77	-10	0.50	5.47
	Aircraft 2	11.0	11.73	-10	0.15	0.88
V_{max}	Aircraft 1	33.5	-5.12	10	0.20	21.85
	Aircraft 2	33.5	1.25	10	0.003	0.18

The first condition to be considered is flight at 16 m/s, max L/D cruise velocity. The tail incidence angle for both aircraft were chosen so that the aircraft is already trimmed at this velocity, so no control input is required and the momentum coefficient $C_{\mu,trim}$=0.

Next, flight at $V=V_{stall}$. For aircraft 1, the free stream velocity is 10.7 m/s, α_{trim}=8.77°, δ=-10° and $C_{\mu,trim}$=0.50. This yields a plasma jet momentum of 5.47 N/m. For aircraft 2, the free stream velocity is 11.0 m/s, α_{trim}=11.73°, δ=-10° and $C_{\mu,trim}$=0.15. This yields a plasma jet momentum of 0.88 N/m

Last, flight at $V=V_{max}$=33.5 m/s is considered. For aircraft 1, α_{trim}=-5.12°, δ=+10° and $C_{\mu,trim}$=0.20. This corresponds to a plasma jet momentum of 21.85 N/m. Given that the horizontal stabilizer span is 0.43 m, the total thrust produced by the plasma jet would be equal to 9.4 N. This is roughly 1.4 times the thrust produced by the aircraft engine at this velocity. Obviously, a more comprehensive analysis would need to take this factor into account. For aircraft 2, α_{trim}=1.25°, δ=+10° and $C_{\mu,trim}$=0.003. This corresponds to a jet momentum of 0.18 N/m.

It should be noted that these high jet strengths are required due to the unique physical operation of jet flaps. A close examination of equations 6-8 shows that increasing the momentum coefficient increases both $\partial C_L/\partial\alpha$ and $\partial C_L/\partial\delta$. A large positive angle of attack requires a negative jet deflection for trim, and a large negative angle of attack requires a positive jet deflection for trim. It is only at small free stream incidence angles that the two terms are complimentary. For an actual application, it would be desirable to make the jet deflection angle as large as is practical. This would allow the aircraft to be trimmed with the smallest possible jet momentum.

E. Current DBD Actuator Effectiveness

As discussed above, the actuator effectiveness is defined as the actuator thrust produced per unit power input. Experimental data shows that this parameter is dependent upon many different factors, including the actuator applied voltage, operating frequency, applied voltage waveform, electrode geometry, dielectric constant and dielectric thickness.

The highest actuator effectiveness achieved in experiment in the present effort is 0.107 mN/W-m. Enloe[1] reports actuator effectiveness as high as 2 mN/W-m. Thomas[2] reports thrust and power data, from which the actuator effectiveness at different operating conditions can be back-calculated to be between 0.2 and 0.4 mN/W-m. Durscher and Roy[4] report an actuator effectiveness of 0.37 mN/W-m using a novel multi-electrode actuator.

It is apparent then that finding a solid trend in these data is difficult. Even more, there is no guarantee that the state-of-the-art actuator effectiveness today will be representative of future plasma actuators that are capable of generating thrust levels 10 to 100 times greater than what is available today. Still, an effectiveness value of 0.4 mN/W-m is representative of the current state-of-the-art.

F. Power Required to Trim the Aircraft

Given the jet momentum required to trim the aircraft and the actuator effectiveness, finding the actuator power requirement is a simple calculation. Equation 13 states that the power required to trim the aircraft is equal to the total jet momentum (momentum input per unit power) divided by the actuator effectiveness.

$$P_{trim} = \frac{F_{trim}}{F/P} \tag{13}$$

Based on the trim analysis above, and assuming an actuator effectiveness of 0.4 mN/W-m, aircraft 1 would require 13.6 kW of power to trim the aircraft at its stall velocity, and 54.6 kW of power to trim the aircraft at its maximum velocity. Aircraft 2 would require 2.22 kW of power to trim the aircraft at stall, and 0.47 kW of power to trim the aircraft at its maximum velocity.

G. Current Energy Storage and System Feasibility

Modern remote aircraft use lithium-ion battery packs to store electrical energy. Manganese-based Li-ion batteries currently achieve energy densities around 180 Watt-hours per kilogram. If it is assumed that 50% of the weight of the aircraft is devoted to batteries, then aircraft 1 stores 270 Watt-hours of energy and aircraft 2 stores 45 Watt-hours. Aircraft 1 would deplete its battery after only 18 seconds of flight at maximum velocity. Aircraft 2 would deplete its battery after 73 seconds of flight at its stall velocity.

This analysis shows that while the current research focus on increasing actuator thrust is necessary, if DBD actuators are to be used for more than stall control applications, increasing actuator effectiveness levels is also critical. Otherwise, the only option is to wait for higher energy density storage to become available.

V. Conclusion

It is well known that DBD actuators are not yet able to produce thrust levels sufficient to implement a control system of the kind investigated in this work. The intent of this work was to determine the amount of power that such a system would require if DBD actuator effectiveness levels remain constant while the thrust levels increase. The analysis above shows that the power requirements would be prohibitive to mounting the system on a small aircraft. Under demanding conditions, results predict that the aircraft are capable of sustaining trimmed flight for only 18 and 73 seconds of flight, respectively. An improvement in duration could be gained by restricting the flight envelope of the aircraft, but this is undesirable.

The experimental portion of the work does offer some promising results. Actuator thrust and power consumption were investigated for a variety of applied voltages and operating frequencies. It was observed that actuator effectiveness increased as the applied voltage was increased. Because increasing actuator voltage levels has so far been the easiest way to increase actuator thrust, it is possible that actuator effectiveness levels will increase along with increasing thrust.

This suggests that future research should focus on ways to increase actuator effectiveness levels as well as increasing actuator thrust levels. Gaining a more fundamental understanding of actuator operating processes is important to achieving this goal. To this end, future modeling and experimental efforts would do well to focus on DBD plasma formation, plasma quenching, and flow acceleration processes. Novel electrode arrangements, voltage waveforms, or dielectric modifications could also be worthwhile.

Investigations should also be performed from the standpoint of aerodynamic flow control. The jet flap analysis performed above is a brute force technique. Flow modification comes only from the actuator direct momentum addition to the flow. DBD actuators are capable of unsteady forcing and vortex generation; further investigation to exploit these effects could allow actuators to have a greater effect at low power levels.

Acknowledgments

The authors would like to thank the NASA-Missouri Space Grant Consortium and Missouri S&T Chancellors Fellowship program for providing student support for this work. We would also like to thank Dr. Jonathon Kimball for helpful insight on the circuit design for operating the plasma actuators. We thank the research team of the Aerospace Plasma Laboratory for helpful suggestions over the course of this work. Further, we thank Bob Hribar, Joe Boze, Ken Schmid, and Mitch Cottrell for assistance with the setup and operation of the experimental component of this work.

References

[1]Enloe, C., McLaughlin, T., Font, G., "Parameterization of Temporal Structure in the Single-Dielectric-Barrier Aerodynamic Plasma Actuator," AIAA Journal 2006, Vol. 44, No. 6, 1127-1136

[2]Thomas, F., Corke, T., Iqbal, M., Kozlov, A., Schatzman, D., "Optimization of Dielectric Barrier Discharge Plasma Actuators for Active Aerodynamic Flow Control," AIAA Journal 2009, Vol. 47, No. 9, 2169-2178

[3]Opaits, D., Neretti, G., Zaidi, S., Shneider, M., Miles, R., Likhanskii, A., Macheret, S., "DBD Plasma Actuators Driven by a Combination of Low Frequency Bias Voltage and Nanosecond Pulses," 46th AIAA Aerospace Sciences Meeting and Exhibit, AIAA 2008-1372, Reno, Nevada 2008

[4]Durscher, R., Roy, S., "Novel Multi-Barrier Plasma Actuators for Increased Thrust," 48th AIAA Aerospace Sciences Meeting Including the New Horizons Forum and Aerospace Exposition, AIAA 2010-965, Orlando, Florida 2010

[5]Enloe, C., McLaughlin, T., VanDyken, R., Kachner, K., Jumper, E., Corke, T., "Mechanisms and Responses of a Single Dielectric Barrier Plasma Actuator: Plasma Morphology," AIAA Journal 2004, Vol. 42, No. 3, 589-594

[6]Stanfield, S., Menart, J., DeJoseph, C., "Spatially Resolved Optical Emission Spectroscopy Measurements within a Single Microdischarge of a Dielectric Barrier Discharge," 48th AIAA Aerospace Sciences Meeting Including the New Horizons Forum and Aerospace Exposition, AIAA 2010-962, Orlando, Florida 2010

[7]Stanfield, S., Menart, J., DeJoseph, C., Kimmel, R., Hayes, J., "Rotational and Vibrational Temperature Distributions for a Dielectric Barrier Discharge in Air," AIAA Journal 2009, Vol. 47, No. 5, 1107-1115

[8]Enloe, C., McLaughlin, T., Gregory, J., Medina, R., Miller, W., "Surface Potential and Electric Field Structure in the Aerodynamic Plasma Actuator," 46th AIAA Aerospace Sciences Meeting and Exhibit, AIAA 2008-1103, Reno, Nevada 2008

[9]Font, G., Enloe, C., Newcomb, J., Teague, A., Vasso, A., McLaughlin, T., "Effects of Oxygen Content on the Behavior of the Dielectric Barrier Discharge Aerodynamic Plasma Actuator," 48th AIAA Aerospace Sciences Meeting Including the New Horizons Forum and Aerospace Exposition, AIAA 2010-545, Orlando, Florida 2010

[10]Poggie, J., Tilmann, C., Flick, P., Silkey, J., Osborne, B., Ervin, G., Maric, D., Mangalam, S., Mangalam, A., "Closed-Loop Stall Control on a Morphing Airfoil Using Hot-Film Sensors and DBD Actuators," 48th AIAA Aerospace Sciences Meeting Including the New Horizons Forum and Aerospace Exposition, AIAA 2010-547, Orlando, Florida 2010

[11]Huang, X., Zhang, X., Gabriel, S., "Bluff Body Noise and Flow Control with Atmospheric Plasma Actuators," 29th AIAA Aeroacoustics Conference, AIAA 2008-3044, Vancouver, British Columbia, Canada 2008

[12]Vincent-Randonnier, A., Larigaldie, S., Magre, P., Sabel'nikov, V., "Experimental Study of a Methane Diffusion Flame Under Dielectric Barrier Discharge Assistance," IEEE Transactions on Plasma Science 2007, Vol. 35, No. 2, 223-232

[13]Benard, N., Bonnet, J., Touchard, G., Moreau, E. "Flow control by dielectric barrier discharge actuators – Jet mixing enhancement," 4th Flow Control Conference, AIAA 2008-3878, Seattle, Washington 2008

[14]Post, M., Corke, T., "Separation Control on High Angle of Attack Airfoil Using Plasma Actuators," AIAA Journal 2004, Vol. 42, No. 11, 2177-2184

[15]Nelson, R., Corke, T., He, C., Othman, H., Matsuno, T., Patel, M., Ng, T., "Modification of the Flow Structure over a UAV Wing for Roll Control," 45th AIAA Aerospace Sciences Meeting and Exhibit, AIAA 2007-884, Reno, Nevada 2007

[16]Huang, J., Corke, T., Thomas, F., "Plasma Actuators for Separation Control of Low-Pressure Turbine Blades," AIAA Journal 2006, Vol. 44, No. 1, 51-57

[17]Ozturk, C., Bolitho, M., Jacob, J., "Parametric Study of Thrust Generation in Plasma Microthrusters," 46th AIAA Aerospace Sciences Meeting and Exhibit, AIAA 2008-539, Reno, Nevada 2008

[18]Morris, C., Corke, T., VanNess, D., Stephens, J., Douville, T., "Tip Clearance Control Using Plasma Actuators," 43rd AIAA Aerospace Sciences Meeting and Exhibit, AIAA 2005-782, Reno, Nevada 2005

[19]Post, M., Plasma Actuators for Separation Control on Stationary and Oscillating Airfoils, South Bend: Notre Dame, 2004, Dissertation

[20]Wang, J., Li, H., Liu, F., Luo, S., "Forebody Asymmetric Load Manipulated by a Horseshoe-Shaped Plasma Actuator," 47th AIAA Aerospace Sciences Meeting Including The New Horizons Forum and Aerospace Exposition, AIAA 2009-904, Orlando, Florida 2009

[21]Post, M., Corke, T., "Flow Control with Single Dielectric Barrier Plasma Actuators," 35th AIAA Fluid Dynamics Conference and Exhibit, AIAA 2005-4630, Toronto, Ontario, Canada 2005

[22]Zhang, P., Liu, A., Wang, J., "Aerodynamic Modification of a NACA 0012 Airfoil by Trailing-Edge Plasma Gurney Flap," AIAA Journal 2009, Vol. 47, No. 10, 2467-2474

[23]Corke, T., Tillotson, D., Patel, M., Su, W., Toledo, W., "Radius Flow Vectoring for Projectile Drag and Steering Control Using Plasma Actuators," 4th Flow Control Conference, AIAA 2008-3769, Seattle, Washington 2008

[24]Corke, T., Enloe, C., Wilkinson, S., "Dielectric Barrier Discharge Plasma Actuators for Flow Control," Annu. Rev. Fluid Mech. 2010, Vol. 42, 505-529

[25]Takagaki, M., Isono S., Nagai, H., Asai, K., "Evaluation of Plasma Actuator Performance in Martian Atmosphere for Applications to Mars airplanes," 4th Flow Control Conference, AIAA 2008-3762, Seattle, Washington 2008

[26]Abe, T., Takizawa, Y., Sato, S., Kimura, N., "Experimental Study for Momentum Transfer in a Dielectric Barrier Discharge Plasma Actuator," AIAA Journal 2008, Vol. 46, No. 9, 2248-2256

[27]Beckwith, T., Marangoni, R., Lienhard, J., Mechanical Measurements, 6th edition,Upper Saddle River: Pearson Prentice Hall, 2007

[28]Spence, D., "The Lift Coefficient of a Thin, Jet-Flapped Wing," Proceedings of the Royal Society of London. Series A, Mathematical and Physical Sciences 1956, Vol. 238, No. 1212

[29]Korbacher, G., "Aerodynamics of Powered High-Lift Systems," Annu. Rev. Fluid Mech. 1974, Vol. 6, 319-357

[30]McKormick, B., Aerodynamics of V/STOL Flight, Academic Press, New York, 1967, chapter 7

[31]Von der Decken, J., "Aerodynamics of Pneumatic High-Lift Devices," AGARD Lecture Series No. 43, 1970

[32]Maskell, E., Spence, D., "A Theory of the Jet Flap in Three Dimensions," Proceedings of the Royal Society of London. Series A, Mathematical and Physical Sciences 1959, Vol. 251

[33]Blakeney, J., Exploratory Study of the Turning Characteristics of a Coanda-Operated Jet Flap, Naval Postgraduate School, 1972, Thesis

[34]Englar, R.J., "Circulation Control Pneumatic Aerodynamics: Blown Force and Moment Augmentation and Modification; Past, Present, & Future," AIAA Fluids 2000 conference and exhibit, AIAA 2000-2541, Denver, Colorado 2000